# Preparation of magnetic calcium phosphate microcarriers loaded with bisphosphate-modified GDF-5 for bottom-up bone tissue engineering

Lisi Li [a,b,1], Yu Pan [a,1], Chengdong Zhang [a,c], Yan Xing [a], Chao Pu [a], Feng Shi [d], Zaijun Yang [d], Jiaping Li [b], Jie Weng [c], Dongqin Xiao [a,*]

[a] Research Institute of Tissue Engineering and Stem Cells, Nanchong Central Hospital, the Second Clinical College of North Sichuan Medical College, Nanchong, Sichuan 637000 China
[b] Department of Complex Tissue Regeneration, MERLN Institute for Technology-Inspired Regenerative Medicine, Maastricht University, Maastricht 6200 MD, the Netherlands
[c] Key Laboratory of Advanced Technologies of Materials (MOE), School of Materials Science and Engineering, Southwest Jiaotong University, Chengdu, Sichuan 610031 China
[d] Collaboration Innovation Center for Tissue Repair Material Engineering Technology, China West Normal University, Nanchong, Sichuan 637002 China

## ARTICLE INFO

## ABSTRACT

For bottom-up bone tissue engineering, microcarriers play crucial roles in serving as scaffolds that provide structural support and environmental cues for cell growth. Studies have demonstrated that the physicochemical properties of microcarriers, such as surface structure and chemistry, have significant effects on cell phenotype. However, current research on microcarriers has primarily focused on hydrogels or polymers, neglecting the exploration of hard materials that mimic the bone tissue environment. In this study, a new facile method to fabricate magnetic calcium phosphate (CaP)-based microcarriers were presented. By this method, magnetic calcium phosphate was obtained without changing the surface nanostructure of CaP microspheres. These magnetic CaP microspheres were utilized as cell-adhesive microcarriers, allowing for cell-guided assembly into spherical microtissue under a relatively low number of cells. However, when using CaP microspheres as microcarriers, only loose aggregates were observed. To enhance the biofunctionality of the magnetic CaP microcarriers, bisphosphonate-modified growth differentiation factor-5 (PGDF-5) were synthesized and selectively deposited onto the magnetic CaP surfaces. Coculture with preosteoblastic cells demonstrated that PGDF-5 modified microcarriers effectively improved cell osteogenic differentiation and angiogenesis, thereby facilitating the formation of highly stable cell spheroids. Collectively, all findings suggest that PGDF-5 modified magnetic CaP microcarriers hold great potential as tools for fabricating bottom-up tissue engineered bone-mimicking tissue.

## 1. Introduction

Nowadays, tissue engineered bone grafts has been regarded as a promising approach to repair large bone defects. Tissue engineering consists of three vital components: cells, scaffolds and bioactive factors. The conventional approach involves seeding cells onto porous scaffolds, which serve as an extracellular matrix (ECM) providing structural support and environmental cues for tissue growth. Many efforts have been made to develop robust scaffolds that mimic ECM structural and composition, aiming to enhance cell function and bone remodeling (Miszuk et al., 2021, Wang et al., 2021). However, when cultured in macroscopic scaffolds, cells in the central region may occur necrosis due to insufficient oxygen and nutrient supply. Additionally, controlling the spatial organization of cells within the scaffold, especially for multiple cell types and complex tissue construction at the micro/nano-scale, poses challenges.

In comparison, bottom-up approaches in tissue engineering show promising potential for fabricating complex tissues with precise spatial

and temporal control at the micro/nano-scale (Feijao et al., 2021, Schmidt et al., 2021). Bottom-up tissue engineering involves building cell-laden microtissues and subsequently assembling them into macroscopic tissues. This approach enables precise spatial control of the microtissues at the cellular level, resulting in a more uniform distribution of seed cells and the assembly of complex tissue structures. Despite these advantages, bottom-up tissue engineering still faces significant challenges in preparing suitable microcarriers to enhance cell function and effectively assemble microtissues into desired macroscopic tissues.

The physicochemical properties of microcarriers, including surface structure, hardness and chemical properties, have important effects on cell phenotype as carriers for cell growth (Leferink et al., 2019, Luo et al., 2019). Therefore, the selection of microcarriers based on tissue characteristics plays a key role in facilitating tissue repair. Calcium phosphate (CaP), as the main inorganic component of human bone tissue, is widely used in bone defect repair due to its good biocompatibility and bioactivity. Especially for nanostructured CaP microspheres, they have demonstrated superior properties in enhancing protein adsorption as well as cell adhesion, proliferation and differentiation (Xiao et al., 2017, Xiao et al., 2020). Accordingly, we propose that CaP microspheres with micro/nano structure would be an ideal cell microcarriers for bone repair.

Cell behavior is not only determined by the surface structure, but also regulated by growth factors involved in bone regeneration. Growth differentiation factor-5 (GDF-5), a member of the bone morphogenetic protein (BMP) family, has attracted increasing attention for its role in bone regeneration (Bae et al., 2014, Zhang et al., 2020). In our previous study, GDF-5 was incorporated with CaP porous scaffolds and implanted *in vivo*, demonstrating that GDF-5 could promote angiogenesis and bone tissue regeneration (Zhang et al., 2020). However, the challenge of low utilization efficiency remains unsolved. To address this, we aim to combine GDF-5 with bisphosphonates, the bone-targeting molecules, to enhance the incorporation ability of growth factors to CaP carriers and achieve effective release of growth factors around bone tissue, thereby promoting bone regeneration.

Additionally, the assembly of isolated single microtissues into desired macroscopic tissue is another major challenge in bottom-up tissue engineering. In recent years, microcarriers have been assembled using microfluidics, acoustic fields, and magnetic fields (Ouyang et al., 2020). In particular, magnetic fields have been widely used in biomedical fields, such as cell sorting, 3D cell culture, local hyperthermia, and clinical imaging (Hori et al., 2021, Gu et al., 2023). The introduction of external magnetic fields can be an effective strategy for achieving particle aggregation and accurate positioning in clinical applications. Therefore, magnetic CaP microcarriers was expected to be used to achieve efficient assembly of microtissues into macroscopic tissues through an external magnetic field.

Based on the above, in order to biomimic the composition and function of microtissues and achieve bottom-up assembly of microtissues into macroscopic tissues, magnetic CaP carriers with enhanced osteoinductive capacity were designed for bone tissue engineering (as illustrated in Fig. 1). Firstly, magnetic CaP microspheres with nanostructures were prepared, and GDF-5 was targetedly deposited onto the CaP surface as microcarriers. Then, the microcarriers were cocultured with preosteoblastic cells to form microtissues, which could be further assembled to form macroscopic tissues with the help of an external magnetic field. Furthermore, the biological functions of the aggregates were investigated *in vitro*.

## 2. Materials and methods

### 2.1. Preparation of magnetic CaP microspheres with nanostructures

CaP microspheres with nanostructures were prepared using the hydrothermal method. Briefly, 0.33 g of $CaCl_2$ and 0.44 g of ethylenediamine tetraacetic acid (EDTA) were successively dissolved in a 30 mL water solution. Then, $Na_2HPO_4$ was dissolved into the solution to give a molar Ca/P ratio of 1.67. Subsequently, 1 g of urea was dissolved into the above solution. The pH of the solution was further adjusted to $\sim$ 2.3 using a dilute HCl solution (volume ratio of HCl: $H_2O$ = 1:2). The resulting solution was then transferred to a 50 mL Teflon-line reactor and autoclaved at 150 °C for 3 h. The product was collected and washed with water and alcohol, and dried at 80 °C for 24 h.

Magnetic $Fe_3O_4$ nanoparticles were synthesized as follows. First, 0.20 g of $FeCl_2 \cdot 4H_2O$ and 0.46 g of $FeCl_3 \cdot 6H_2O$ were dissolved in 40 mL of water. Next, 5 mL of turpentine was added onto the water surface to prevent air oxidation of iron ions. Subsequently, 3.5 mL of ammonia was added into the water under the protection of nitrogen. The resulting solution was then transferred to 100 mL autoclave vessels and heated at 120 °C for 20 h. The product was collected and washed with alcohol and water, and dried under vacuum.

For the preparation of magnetic CaP microspheres, CaP microspheres
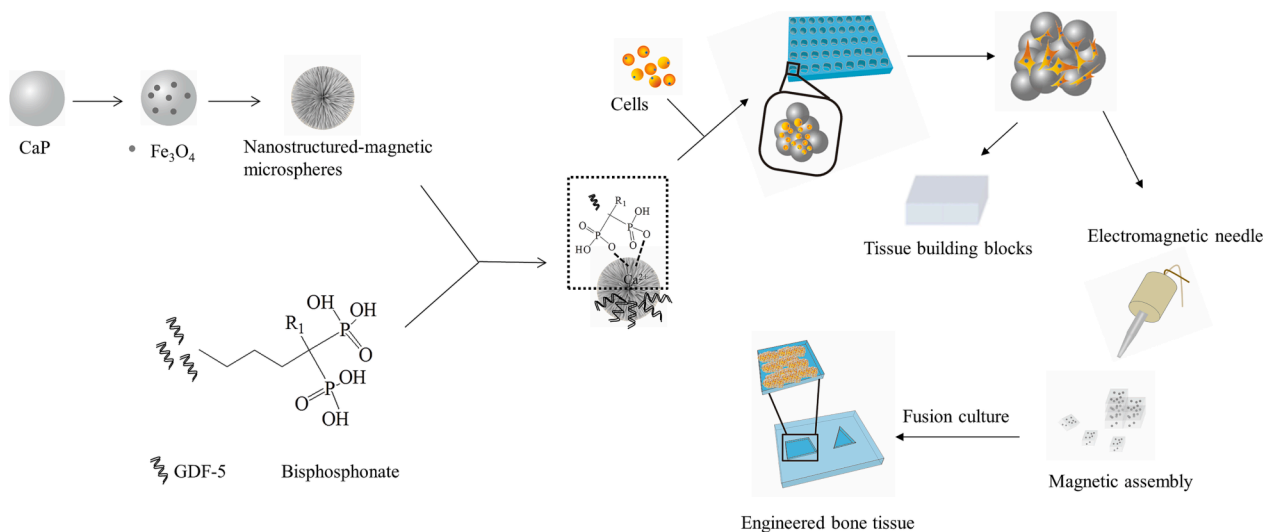


**Fig. 1.** Schematic diagram of experimental design. First, CaP microspheres with nanostructures were incorporated with magnetic nanoparticles to form magnetic CaP microcarriers. Bisphosphonate-modified GDF-5 was synthesized and incorporated with CaP microcarriers. Then, the obtained magnetic CaP microcarriers were cocultured with MC3T3-E1 cells to form cell aggregates. Subsequently, the cell aggregates were assembled into larger ones under the assistant of an external magnetic field for fabrication of engineered bone tissue.

were mixed with $Fe_3O_4$ nanoparticles at a $CaP/Fe_3O_4$ mass ratio of 5:1 under ultrasonic condition (600 w, 5 min). The resulting mixture was separated by a magnet and washed using water and ethanol, and further dried at 80 °C for 12 h. The obtained sample was named as $CaP/Fe_3O_4$.

The obtained samples were observed using scanning electron microscope (SEM, JSM-7610F, JEOL) equipped with energy dispersive spectrometer (EDS) and transmission electron microscopy (TEM, FEI Talos F200S, Thermo). The composition and crystalline phase were analyzed using Fourier transform infrared spectroscopy (FTIR, Spectrum2, PerkinElmer), X-ray photoelectron spectroscopy (XPS, Fisher Scientific Escalab 250 Xi, Thermo) and X-ray diffraction (XRD, D8 Advance, Bruker). The magnetic properties of the particles were characterized by vibrating sample magnetometer (VSM, 8600, Lakeshore).

## 2.2. Preparation of GDF-5 conjugated with bisphosphonate

The preparation of GDF-5 conjugated with bisphosphonate was divided into following steps. Firstly, the –$NH_2$ groups in GDF-5 were reacted with N-succinimidyl-3-(2-pyridyldithio) propionate (SPDP) to introduce disulfide groups to the protein. Secondly, the –$NH_2$ groups in bisphosphonate were converted to -SH by using 2-iminothiolane (2-IT). Finally, the preactivated GDF-5 was combined with thiolated bisphosphonate to form GDF-5/bisphosphonate conjugate. Briefly, 0.25 g of N-ethylmaleimide (NEM) was dissolved in a 20 mL solution of dimethylformamide (DMF). Then, a 10 mL solution of GDF-5 (Abcam, 100 µg/ml in 0.1 M phosphate buffer, pH = 7.4) was incubated in the NEM solution for 30 min. After centrifugation, the NEM-treated GDF-5 was incubated for 2 h in a 10 mL solution of 3-(2-pyriddisulphide) propionate N-succinimide ester (SPDP), which was initially dissolved in a DMF solution (50 mM). The unreacted reagents were removed by dialysis in a phosphate buffer solution (PBS). Separately, pamidronate sodium (20 mM in PBS) was incubated with 2-iminothiolane hydrochloride (100 mM in PBS) for 2 h at a volume ratio of 1:1. Subsequently, SPDP-treated GDF-5 solution was added into the solution with equal volumes and incubated for 1 h. The unreacted reagent was removed by dialysis in a carbonate buffer (100 mM) and water. The obtained powder was defined as PGDF-5. All the above reactions were performed at room temperature. The obtained powder was characterized for group composition using FTIR and circular dichroism (CD, Jasco J-1500, Hachioji), and for protein molecular weight using Sodium Dodecyl Sulfate-polyacrylamide gel electrophoresis (SDS-PAGE).

## 2.3. Preparation of magnetic CaP microspheres loaded with PDGF-5

To prepare magnetic CaP microspheres loaded with PDGF-5, 5 mg of magnetic CaP microspheres were placed in a 5 mL solution of PDGF-5 or GDF-5 (400 ng/ml, diluted with PBS) and shaken for 3 h. After centrifugation (7000 rpm, 10 min), the samples were collected and washed with PBS. The protein concentration in the supernatant was measured using a GDF-5 enzyme linked immunosorbent assay (ELISA) kit (Zeye Biotechnology, Shanghai, China). The GDF-5 concentration bound to the CaP microspheres was calculated using the following formula: (original protein concentration-supernatant protein concentration)/original protein concentration*100 %. To investigate the stability of PGDF-5/microspheres, the collected samples were immersed into a 50 mM Tris buffer (pH = 7.4) containing 0 or 5 mM cysteine. After shaking for predetermined times, the supernatant was collected and determined using a GDF-5 ELISA kit.

## 2.4. Formation of cell/microcarrier aggregates

Murine MC3T3-E1 preosteoblasts were purchased from the American Type Culture Collection (ATCC) and cultured in Alpha-Minimum Essential Medium (α-MEM, Gibco) supplemented with 10 % fetal bovine serum (FBS, Gibco) and 1 % penicillin–streptomycin (37 °C, 5 % $CO_2$). The culture medium was changed every 2 d. Cells were detached

with trypsin when a confluency was reached 70–80 %.

To create cell-repellent surfaces, a solution of agarose in water (1 wt %; UltraPure, Invitrogen) was heated in a water bath to 80 °C and coated onto culture wells. Microcarriers and cells were suspended in the α-MEM at different ratios and added to the culture plates. The morphology of cell/microcarrier aggregates was observed using a light microscope (DM750, Leica). The average diameter of the aggregates was determined using Image J. Based on the microcarriers, the experiment groups were named as CaP, $CaP/Fe_3O_4$, $CaP/Fe_3O_4/GDF-5$, $CaP/Fe_3O_4/PGDF-5$.

After culture for 1, 4 and 7 d, cell proliferation was determined using cell counting kits (CCK-8, Beyotime, China). Additionally, after culture for 1, 7 and 14 d, the aggregates were observed and images were captured using a light microscope. After culture for 4 d, the aggregates were fixed using 2.5 % glutaraldehyde at 4℃ overnight, and further dehydrated in graded ethanol (50 %, 70 %, 80 %, 90 %, 100 %) followed by air-drying. Then, the aggregates were gold sputter-coated and observed using SEM. After culture for 14 d, the cell aggregates were washed using PBS and stained with a mixture of 2 µmol/L calcein-AM and 4 µmol/L propidium iodide (PI). The cells were then observed under a fluorescence microscope (Ts2, Nikon).

## 2.5. Osteogenic capability of the cell/microcarriers aggregates

After culture for 1 d, the medium was replaced with osteogenic differentiation medium (α-MEM containing 10 % FBS, 10 mM β-glycerophosphate, 100 nM dexamethasone, and 50 µg/ml of ascorbic acid). The culture medium was changed every 2 d. After culture for 7 d, the alkaline phosphatase (ALP) activity of the cell aggregates was measured using an ALP microplate test kit (P0321, Beyotime, China). After culture for 7 d, the cells were then immunofluorescently stained using iFluor488-labeled phalloidin, 2-(4-Amidinophenyl)-6-indolecarbamidine dihydrochloride (DAPI) and antibodies against osteopontin (OPN) and osteocalcin (OCN). The stained cells were observed under a fluorescence microscope and semi-quantified using Image J software.

## 2.6. Endothelial cells coculture with microcarriers extract

To determine the angiogenesis capability of the microcarriers, human umbilical vein endothelial cells (HUVECs, $2 \times 10^4$ per well) were cocultured with microcarrier extract in endothelia cell growth medium. The microcarrier extract was collected from the supernatant of the culture medium after coculture of microcarriers with MC3T3-E1 for 2 d. After culture with microcarrier extract for 4 d, HUVECs were immunofluorescently stained using iFluor488-labeled phalloidin, DAPI and an antibody against vascular endothelial growth factor (VEGFA, Abcam). The stained cells were observed using a fluorescence microscope and semi-quantified using Image J software.

Additionally, HUVECs ($5 \times 10^3$ per well) were seeded onto Matrigel-coated 96-well plates and cocultured with different microcarrier extract for a tube formation assay. After 3 and 9 h, the cells were observed using an inverted microscope. The number of meshes, indicating the ability of cells to form tubes, was quantified using Image J software.

HUVECs ($5 \times 10^3$ per well) were seeded onto 24-well plates and cocultured with different microcarrier extracts for the scratch assay. After cell confluence was reached 100 %, the surface was scratched using a 200 µL pipette tip. Subsequently, the culture medium was replaced with microcarrier extract without FBS. After culture for 0 and 24 h, cell migration was observed using a light microscope and quantified using Image J software.

## 2.7. Statistical analysis

All data were presented as mean ± standard deviation and further analyzed using analysis of variance (ANOVA) followed by Tukey multiple comparison tests. A p-value < 0.05 was considered significant difference.

## 3. Results and discussion

### 3.1. Preparation and characterization of magnetic CaP microspheres

For synthesis of magnetic CaP, a hydrothermal method was used to produce CaP microspheres using $CaCl_2$ as the calcium source, and $Na_2HPO_4$ as the phosphorous source. To prepare microspheres with good dispersibility and uniformity, the organic chelator EDTA was added to regulate the growth of CaP crystals to obtain the desired morphology and size of CaP particles (Qi et al., 2020, Yao et al., 2021). Additionally, the incorporation of $Fe_3O_4$ nanoparticles onto the CaP surface, was expected to confer magnetic properties to the microspheres and facilitate their rapid aggregation by using an external magnetic field.

The morphology of the prepared $Fe_3O_4$, CaP and $CaP/Fe_3O_4$ particles was shown in Fig. 2. The prepared magnetic nanoparticles exhibited uniform microspheres with an average diameter of ~ 21 nm (Fig. 2A and Supplementary Fig. S1a). High-resolution TEM showed that, the lattice fringes had interplanar spacings of 0.291 nm and 0.251 nm, corresponding to the (2 2 0) and (3 1 1) planes of $Fe_3O_4$ (JCPDS 01–085-1436), respectively. For CaP synthesis, ribbon-like crystals formed without EDTA presence (Supplementary Fig. S1c). In comparison, at 0.05 M EDTA, the product was composed of microspheres (average diameter: ~ 8 μm) with nanorods on the surface (Fig. 2B and Supplementary Fig. S1b). Further increase of EDTA concentration to 0.1 M resulted in the formation of smaller microspheres (average diameter: ~2 μm) with nanorods on the surface. The above results indicated that EDTA concentration played key roles in regulating the morphology and size of CaP microspheres. Previous studies have demonstrated that EDTA can chelate with $Ca^{2+}$ and further inhibit the c-axis growth of CaP whiskers, thus leading the formation of CaP microspheres (Zarkesh et al., 2017, Yao et al., 2021). Higher EDTA concentration resulted in a rapid decrease in free $Ca^{2+}$, which restricted the CaP growth and led to formation of smaller CaP microspheres. In this study, larger microspheres

prepared at 0.05 M EDTA were chosen for further study as microcarriers for cell aggregates. The CaP microspheres were then mixed with $Fe_3O_4$ at a mass ratio of 5:1 under ultrasonic conditions, resulting in a color change from white to dark brown in the solution (Supplementary Fig. S1d). The microspheres could be easily separated from the solution using an external magnet (Fig. 2C). SEM images showed that the CaP/ $Fe_3O_4$ mixture had uniform particle size and morphology, similar to the CaP microspheres. However, the nanostructures on the microsphere appeared less distinct. EDS analysis (Fig. 2d) confirmed that the microspheres were mainly composed of Ca、P and O, with small amounts of uniformly distributed Fe on the surface. Semi-quantitative analysis of EDS data indicated a Ca/P ratio of ~ 1.5, suggesting the formation of calcium-deficient apatite. TEM images (Supplementary Fig. S2) showed that the surface of the microspheres consisted of nanorods (length: ~200 nm, width: ~40 nm) and nanoparticles (diameter: ~ 20 nm). The lattice fringes of the nanoparticles corresponded to the (3 1 1) planes of $Fe_3O_4$ with an interplanar spacing of 0.251 nm, while the lattice fringes of the nanorods corresponded to the (0 0 2) plane of hydroxyapatite (HA) with an interplanar spacing of 0.338 nm. Thus, all the results indicated that CaP microspheres with magnetic properties were successfully prepared using a simple ultrasonic method. Noteworthily, the mass ratio between CaP and $Fe_3O_4$ is a key factor affecting the magnetic property of CaP particles. When the mass ratio of $CaP/Fe_3O_4$ was 7:1, a portion of the mixture was unable to be absorbed by the external magnet and was deposited onto the bottom. At a mass ratio of 3:1, there was a significant decrease in cell proliferation compared to pure CaP and $CaP/Fe_3O_4$ (5:1), indicating potential cell toxicity due to the high $Fe_3O_4$ amount present in the magnetic CaP particles (Supplementary Fig. S3). Based on these findings, the mass ratio of $CaP/Fe_3O_4$ was fixed at 5:1 for further investigation.

The prepared samples CaP, $Fe_3O_4$ and $CaP/Fe_3O_4$ were further characterized using XRD and FTIR. XRD patterns of CaP microspheres and $Fe_3O_4$ nanoparticles (Fig. 3a) matched with the standard diffraction pattern of HA (JCPDS 09–0432) and $Fe_3O_4$ (JCPDS 01–085-1436),
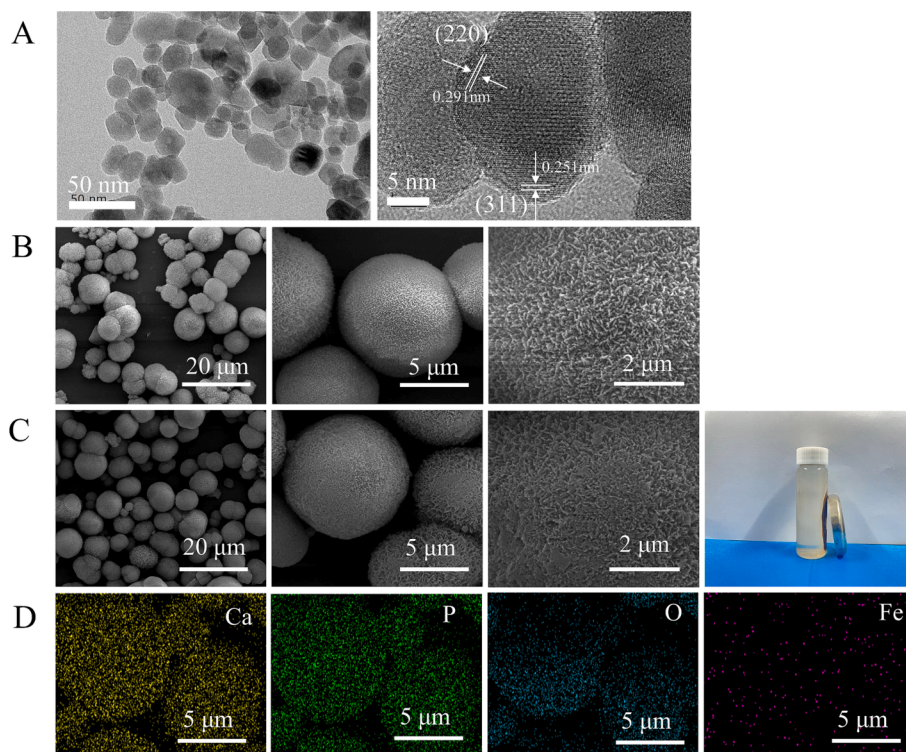


**Fig. 2.** (A) TEM images of $Fe_3O_4$ nanoparticles, (B) SEM images of CaP microspheres (×5 000, ×20, 000, ×60, 000), (C) SEM images of $CaP/Fe_3O_4$ microspheres (×5 000, ×20, 000, ×60, 000) and the photograph of isolation of $CaP/Fe_3O_4$ particles from solution using external magnet, (D) the elements distribution on the surface of $CaP/Fe_3O_4$ microspheres.
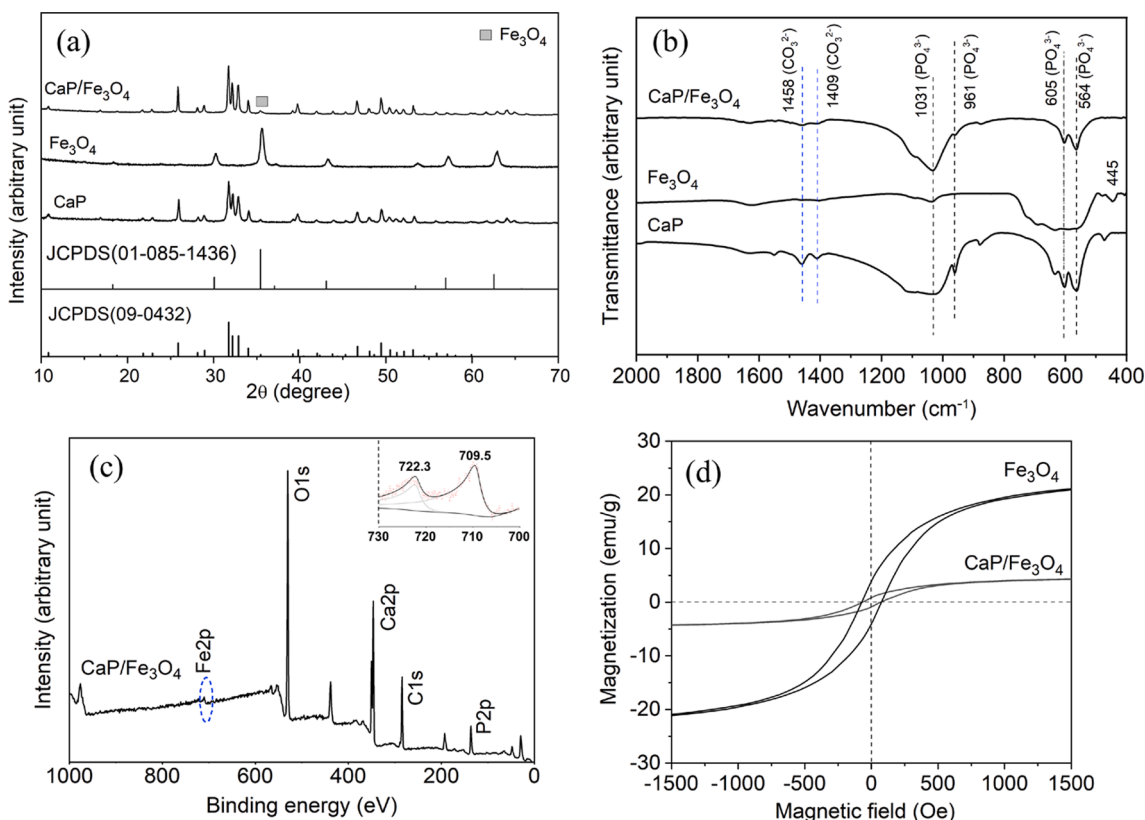
**Fig. 3.** (a) XRD patterns and (b) FTIR spectra of CaP, $Fe_3O_4$ and $CaP/Fe_3O_4$, (c) XPS spectrum of $CaP/Fe_3O_4$, inlet, high-resolution XPS spectrum of Fe, (d) magnetization curves of $Fe_3O_4$ and $CaP/Fe_3O_4$.

respectively. The XRD patterns of $CaP/Fe_3O_4$ exhibited major peaks corresponding to HA and a minor peak at $35.5°$ corresponding to (3 1 1) faces of $Fe_3O_4$, which were consistent with the TEM results (Supplementary Fig.S2). In the FTIR spectra (Fig. 3b), the bands at 564 and 605 $cm^{-1}$ were assigned to phosphate bending and the bands at 961 and 1031 $cm^{-1}$ were assigned to phosphate stretching, corresponding with those of HA (Koutsopoulos, 2002). Additionally, the weak band at 1409 $cm^{-1}$ was assigned to $CO_3^{2-}$ replacing $PO_4^{3-}$ and the band at 1458 $cm^{-1}$ was assigned to $CO_3^{2-}$ replacing $OH^-$, indicating the formation of AB-type carbonate HA (Gibson and Bonfield, 2002, Safarzadeh et al., 2019). Furthermore, the band at 605 $cm^{-1}$ was assigned to the vibration of Fe-O tetrahedral bond, while the band at 445 $cm^{-1}$ was assigned to the vibration of Fe-O octahedral bond (Kumar et al., 2015, Husain et al., 2019). The co-existence of octahedral and tetrahedral Fe-O bands in the FTIR spectra confirmed the presence of $Fe_3O_4$ phase, consistent with the XRD results. However, in the FTIR spectrum of $CaP/Fe_3O_4$, $Fe_3O_4$ could not be distinguished due to the overlay peak at 605 $cm^{-1}$. Thus, XPS measurement was used to further identify the presence of $Fe_3O_4$ in $CaP/Fe_3O_4$. The result (Fig. 3c) revealed characteristic peaks of Ca, P, O, C and Fe. The high-resolution spectrum demonstrated that the Fe2p spectrum comprised one doublet at 709.5 eV ($Fe2p_{3/2}$) and 722.3 eV ($Fe2p_{1/2}$), which were consistent with the binding energies of $Fe_3O_4$ in previous studies (Hu et al., 2006, Raha and Ahmaruzzaman, 2021). Moreover, the magnetization hysteresis curves of $Fe_3O_4$ and $CaP/Fe_3O_4$ were shown in Fig. 3d. Both $Fe_3O_4$ and $CaP/Fe_3O_4$ exhibited hysteresis loops, indicating ferromagnetic behavior. The magnetic saturation and coercivity values for $Fe_3O_4$ were 25 emu/g and 69 Oe, respectively. $CaP/Fe_3O_4$ exhibited magnetic saturation of 5 emu/g and coercivity of 56 Oe. The reduced magnetic saturation could be attributed to the decreased mass ratio of $Fe_3O_4$. According to magnetization curves, the mass ratio of $CaP/Fe_3O_4$ was calculated as 4.88, which was consistent with the material design mentioned in section 2.1 (the mass ratio of $CaP/Fe_3O_4$ was fixed at 5:1).

These results confirmed the successful preparation of magnetically nanostructured CaP microspheres using a simple method, while maintaining the original CaP particle morphology to a great extent. Furthermore, the combination of $Fe_3O_4$ nanoparticles and CaP microspheres exhibited good stability. Even after being immersed in a water solution for 21 d, the microspheres still retained their magnetic properties. This interaction was probably attributed to the electrostatic attraction between the negative charge on the surface of $Fe_3O_4$ nanoparticles (zeta potential: –32 mV) and the positive charge derived from $Ca^{2+}$ on the surface of CaP microspheres. The pH value of the synthesized solution was 10 ~ 11, which resulted in the surface of $Fe_3O_4$ having a negative charge potential due to the dissociation of Fe-OH and the formation of $Fe-O^-$ (Reddy et al., 2014). In addition, the nanorod structures on CaP microspheres preferentially grew along the c-axis direction and exposed many $Ca^{2+}$ sites, which benefited for the attraction of more negative $Fe_3O_4$ nanoparticles (Xiao et al., 2015).

### 3.2. Preparation and characterization of magnetic CaP loaded with PGDF-5

With the rapid development of tissue engineering technology, the significant advantages of growth factors in promoting bone tissue repair have attracted great attention. However, there are concerns regarding the high cost and potential side-effects, such as ectopic osteogenesis or vascularization) (Oryan et al., 2014, James et al., 2016). Therefore, it is crucial to improve the targeted deposition of growth factors onto bone tissue. Sodium pamidronate, as a bisphosphonate, not only has good bone affinity, but also contains amino groups on the side chain, which allows for chemical functional modification. This makes it an effective approach to use bisphosphonate to modify growth factors, enhancing bone targeting and reducing the required dose. In this study, sodium pamidronate was conjugated to GDF-5 using SPDP as a crosslinking agent. The FTIR spectra (Fig. 4a) of PGDF-5 showed bands at 923, 1073
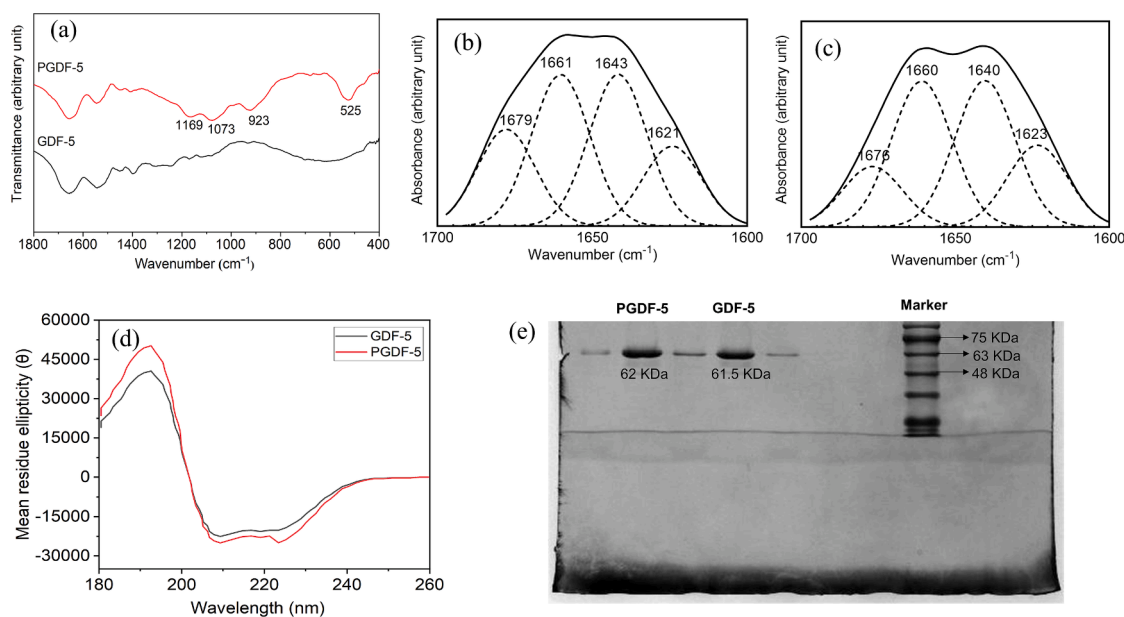
**Fig. 4.** (a) FTIR spectra of GDF-5 and PGDF-5, curve-fitted secondary derivative amine I spectra of (b) GDF-5 and (c) PGDF-5, (d) the CD spectra of GDF-5 and PGDF-5 in UV regions, (e) protein molecular weight of GDF-5 and PGDF-5 using SDS-PAGE.

and 1169 cm$^{-1}$, which corresponded to the stretching vibrations of the phosphate group (Alipour et al., 2022). In addition, a band at 525 cm$^{-1}$ assigned to disulfide (Safarpour et al., 2017) indicated the successful conjugation between GDF-5 and bisphosphonate through a disulfide linkage. Deconvolution, a mathematical approach, was used to enhance the resolution of the amide I spectral region and resolve the individual bands into constituent bands assigned to protein secondary structure. The deconvolutions of GDF-5 and PGDF-5 in the amide I spectra region (1600–1700 cm$^{-1}$) were shown Fig. 4b and c, respectively. In GDF-5 spectrum, data analysis showed that the relative area near 1621 cm$^{-1}$ assigned to β-sheet accounted for 16.6 %, the area near 1643 cm$^{-1}$ assigned to random coil accounted for 31.5 %, the area near 1661 cm$^{-1}$ assigned to α-helix accounted for 31.5 % and the area near 1679 cm$^{-1}$ assigned to β-turn accounted for 20.4 %. In the PGDF-5 spectrum, β-sheet (the area near 1623 cm$^{-1}$) accounted for 18.8 %, random coil (the area near 1640 cm$^{-1}$) accounted for 33.7 %, α-helix (the area near 1660 cm$^{-1}$) accounted for 33.6 % and β-turn (the area near 1676 cm$^{-1}$) accounted for 13.9 %. A similar trend was observed in the CD spectra of GDF-5 and PGDF-5 (Fig. 4d and Table S1). These results indicated that the secondary structure of bisphosphonate-modified GDF-5 was not significantly different from pristine GDF-5, suggesting the high bioactivity of PGDF-5. The SDS-PAGE analysis (Fig. 4e) suggested that the molecular weight of GDF-5 and PGDF-5 had no significantly difference, demonstrating that the SPDP used in PGDF-5 synthesis process did not induce protein–protein linkage. In this process, SPDP, a heterobifunctional cross-linking agent, first reacted with the primary amino group on the protein side chain to introduce pyridyl dithio groups. Meanwhile, amino radicals on pamidronate sodium reacted with 2-IT to generate sulfhydryl groups. The conjugates between GDF-5 and pamidronate sodium were then formed through the exchange of sulfhydryl groups on pamidronate sodium and disulfide bonds on proteins (illustrated as Supplementary Fig. S4) (Wright et al., 2006). Compared with other commonly used protein cross-linking reagents (e.g., glutaraldehyde, carbodiimide, etc.), the conjugation reaction using SPDP is easy to control and has fewer side-effects (e.g., protein self-cross-linking).

Additionally, the magnetic CaP binding assay (Supplementary Fig. S5a) showed that GDF-5 gave a relatively low binding (~33 %) whereas PGDF-5 gave a much higher binding (~78 %). These results indicated that bisphosphonate modification significantly enhanced the mineral affinity of GDF-5. Moreover, the protein release amount were measured

after shaking for 24 h, with ~ 5.0 ng released at 0 mM cysteine and ~ 22.0 ng released at 5 mM cysteine (Supplementary Fig.S5b). This suggested that the presence of cysteine benefited protein release. The cumulative release curves (Supplementary Fig.S5c) demonstrated that protein release in a cysteine-containing solution was significantly faster than in a solution without cysteine within 15 d. This was probably attributed to the presence of -SH groups in cysteine molecule, which could break disulfide bonds in PGDF-5, leading to protein dissociation from the bisphosphonate (Mthembu et al., 2020). Therefore, the bisphosphonate-modified protein not only retained the bioactivity, but could also be released through reductive cleavage of disulfide linkages, such as cysteine. Considering that the environment surrounding bone defects is rich in reductive agents, such as peroxyl free radicals and ROS, which facilitate disulfide bonds cleavage (Giles et al., 2001). Therefore, utilizing SPDP to conjugate bisphosphonate and GDF-5 is an effective method for improving protein affinity to bone mineral.

### 3.3. Cell-guided assembly of CaP-based microcarriers and formation of cell/microcarrier aggregation

To fabricate biomimetic modular bone tissue at micro-nano scale and develop cell/carrier aggregates for bottom-up bone tissue engineering, cells were cocultured with CaP-based microcarriers on a cell-repellent agarose coating. The effect of cell density on aggregate formation was investigated by adding varying cell densities ($1 \times 10^3$, $2 \times 10^3$ and $4 \times 10^3$ per well) to 96-well plates, while keeping the magnetic CaP concentration at 3 mg/ml (200 μL per well). With time increase, the cells guided the assembly of magnetic CaP particles to form aggregates, which became smaller for all groups over time (Supplementary Fig. S6a). However, at low cell density ($1 \times 10^3$ per well), the aggregates formed after culture of 14 d exhibited irregular and loose structures, which would collapse with mild vibration. In contrast, at higher cell densities ($2 \times 10^3$ and $4 \times 10^3$ per well), the aggregates exhibited compact spheroids with sufficient mechanical stability, allowing them to be moved using tweezers. The effect of particle density on aggregate formation was also investigated at a fixed cell density of $2 \times 10^3$ per well (Supplementary Fig. S6b). At low particle densities (3 mg/ml and 5 mg/ml), smaller spherical aggregates with mechanical stability formed over time. Furthermore, the aggregate diameter significantly increased (1.1 mm vs 1.7 mm) with higher particle density after culture of 14 d.

However, at high particle density (7 mg/ml), irregular and loose cellular aggregates formed after culture of 14 d. Therefore, higher cell-to-particle ratios facilitated the formation of 3D cell/microcarrier spheroids, while a relatively higher particle-to-cell ratio resulted in larger spheroids. To achieve faster formation of aggregates with mechanical stability, a cell density of $2 \times 10^3$ per well and a particle density of 5 mg/ml were fixed for the subsequent study.

Fig. 5A showed the gross images of cells cocultured with different microcarriers at 1, 7 and 14 d. With time increase, the dispersed particles in the solution assembled into spheroids with the guidance of the cells, starting from flat cellular aggregates. At day 7 and 14 d, the size of loose aggregate for CaP microcarriers slightly reduced ($\sim 2.1$ mm vs 2.0 mm), while the aggregate diameter significantly decreased for the other three groups as time prolonged. At day 14, the aggregate diameter was $\sim 1.5$ mm for $CaP/Fe_3O_4$ microcarriers, $\sim 1.3$ mm for $CaP/Fe_3O_4/GDF-5$ microcarriers and $\sim 1.1$ mm for $CaP/Fe_3O_4/PGDF-5$ microcarriers. Moreover, all three groups exhibited a spherical morphology and sufficient mechanical stability to be transferred using tweezers. After culture of 14 d, the cell live/dead fluorescent microscopy images of the cells (Fig. 5B) showed the presence of both live (green) and dead (red) cells in all four groups, with the live cells being the majority. The size of the cell aggregates showed a decreasing trend as followed: $CaP > CaP/Fe_3O_4 > CaP/Fe_3O_4/GDF-5 > CaP/Fe_3O_4/PGDF-5$, which corresponded with the gross morphology observed in Fig. 5A. The CaP microcarriers showed a loose structure and flat morphology, while the other three groups had spherical morphology. The spheroids formed by the $CaP/Fe_3O_4/GDF-5$ and $CaP/Fe_3O_4/PGDF-5$ groups had compact cellular aggregates with smaller size and strong mechanical stability. Most of cells in the spheroids were viable. Previous studies have shown that bottom-up techniques, where cells replaced between micro-objects, allow homogeneous cell distribution and easy access to nutrients for internal cells (Griffin et al., 2015, Leferink et al., 2019). Therefore, the cells in the spheroids assembled using magnetic CaP-based microcarrier maintained good viability. Other studies have used concave non-adherent surfaces (Costa et al., 2014, Tajima and Tabata, 2018) or centrifugation (Froehlich et al., 2016) to prepare spherical cellular aggregates. In this study, magnetic CaP-based carriers were used to successfully form spheroids with a diameter of $\sim 1$ mm after culture of 14 d, indicating that the addition of magnetic CaP microcarriers could be an effective strategy for constructing cell spheroids. Previous studies on cell-only aggregates required a high number of cells to form submillimeter-sized tissue (Leung and Sefton, 2010, Dikina et al., 2018). However, with the assistance of magnetic CaP microcarriers, larger-sized tissue spheroids were formed with a relatively low number of cells. Particularly, the $CaP/Fe_3O_4/GDF-5$ and $CaP/Fe_3O_4/PGDF-5$ microcarriers exhibited strong mechanical stability in the formed spheroids.

### 3.4. Cell proliferation and osteogenic differentiation during co-culture with microcarriers

To investigate the effects of microcarriers on cell proliferation and osteogenic activity, MC3T3-E1 cells were cocultured with CaP-based microcarriers on a cell-repellent agarose coating. CCK-8 assay (Fig. 6A) showed that the cell number increased over time for all groups. However, on day 1, there were no significant differences among the four groups. On day 4, the cell number on $CaP/Fe_3O_4/GDF-5$ microcarriers were significantly higher than that on CaP microcarriers (p = 0.02). On day 7, the cell number on $CaP/Fe_3O_4/PGDF-5$ was significantly higher than that on $CaP/Fe_3O_4$ (p = 0.009). CCK-8 results indicated that the addition of growth factors, including GDF-5 and PGDF-5, had a positive effect on cell proliferation. On day 4, SEM images (Supplementary Fig. S7) demonstrated the presence of microcarrier/cell aggregates. However, CaP microcarriers assembly by cell guidance appeared flat and loosely, whereas the other three magnetic microcarriers exhibited complete integration under a dense layer of cells. Furthermore, the assembly of the magnetic microcarriers appeared more three-dimensional, with surfaces that were either convex or concave.

Cellular osteogenic activity was determined by ALP activity and immunofluorescence staining after co-culture of 7 d. Cellular ALP activity (Fig. 6B) on different microcarriers showed a trend of $CaP < CaP/Fe_3O_4 < CaP/Fe_3O_4/GDF-5 < CaP/Fe_3O_4/PGDF-5$. The differences between all pairs of groups were statistically significant (p < 0.0001). Specifically, the ALP level on $CaP/Fe_3O_4/PGDF-5$ microcarriers was $\sim 43\%$ higher than that on $CaP/Fe_3O_4/GDF-5$ microcarriers, $\sim 87\%$ higher than that on $CaP/Fe_3O_4$ microcarriers, and about 4.8-fold higher than that on CaP microcarriers. In addition, the protein expressions including OCN and OPN were evaluated using immunofluorescence staining (Fig. 6C). The cell nuclei were stained into blue using DAPI, while F-actin was stained green using iFluor488-labeled phalloidin, and OCN/OPN were immunostained red. For all groups, the actin filaments formed intricate networks. These filament networks on the microcarriers' surface likely contribute to the mechanical forces responsible for microcarriers aggregation and cell motility (Achard et al., 2010, Svitkina, 2018). Immunofluorescent staining of osteogenic protein
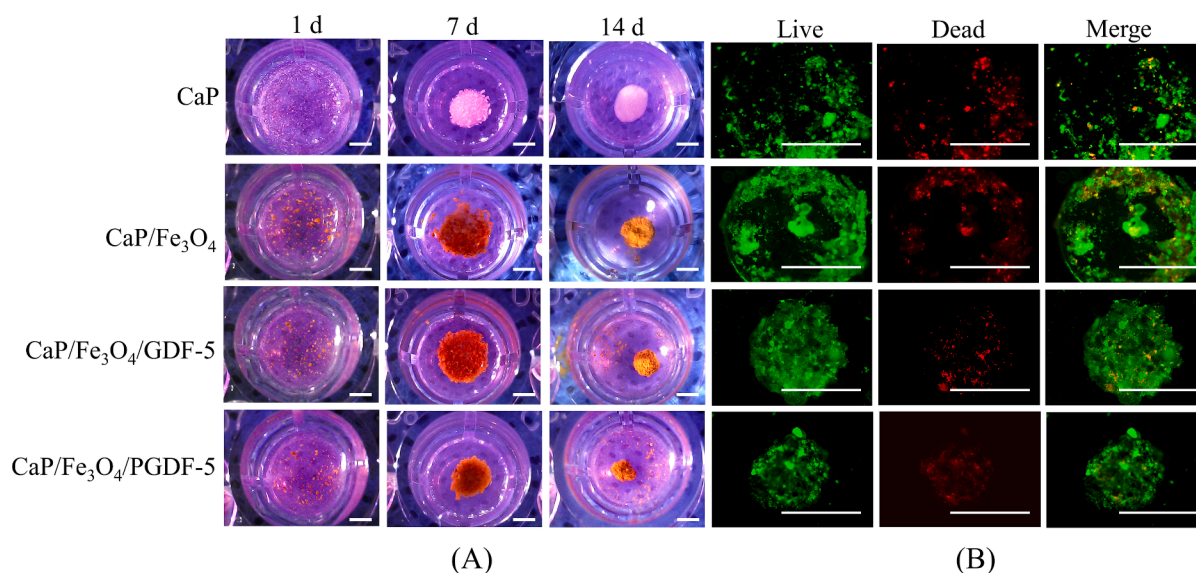


**Fig. 5.** (A) Gross morphology of cells co-cultured with different carriers at different days (scale bar = 1 mm), (B) Calcein-AM/PI staninings of cell/carrier aggregates (scale bar = 1 mm). Green represents live cells while red represents dead cells.
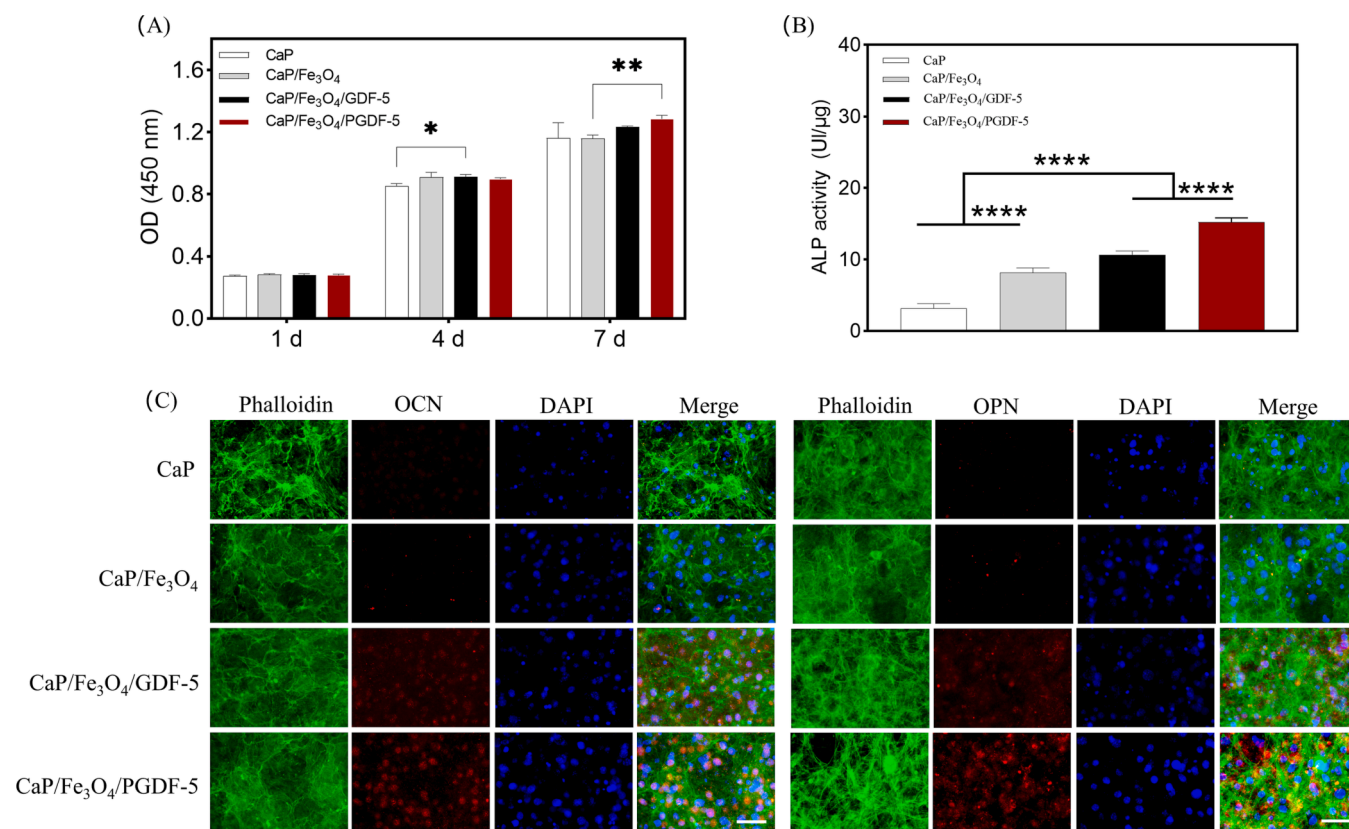
**Fig. 6.** (A) The proliferation of MC3T3-E1 cells co-cultured with CaP-based microcarriers at 1, 4 and 7 d, (B) the ALP activity of cells co-cultured with CaP-based microcarriers at 7 d, (C) immunofluorescent stainings of osteogenic makers including OCN and OPN after co-culture of 7 d. F-actin was stained with iFluor488-labeled phalloidin (green), cell nuclei was stained using DAPI (blue) and OPN/OCN were immunostained red (scale bar = 100 μm). * represents p < 0.05, ** represents p < 0.01, **** represents p < 0.0001.

markers showed similar results for OCN and OPN. Most of the cells on CaP/Fe$_3$O$_4$/GDF-5 and CaP/Fe$_3$O$_4$/PGDF-5 microcarriers expressed OCN and OPN, while only a small number of cells on CaP and CaP/Fe$_3$O$_4$ microcarriers expressed these proteins. Correspondingly, the semi-quantitative analysis (Supplementary Fig.S8) showed that OCN expression was the highest in the CaP/Fe$_3$O$_4$/PGDF-5 group, followed by the CaP/Fe$_3$O$_4$/GDF-5 group, while the lowest expression was observed in the CaP and CaP/Fe$_3$O$_4$ groups. The groups of CaP/Fe$_3$O$_4$/GDF-5 and CaP/Fe$_3$O$_4$/PGDF-5 exhibited significantly higher OPN expressions compared to the groups of CaP and CaP/Fe$_3$O$_4$. ALP is considered as an early biomarker for osteoblastic phenotype, whereas OCN and OPN are considered late biomarker for biomineralization and osteogenic differentiation. Overall, the results proved that the incorporation of growth factors (including GDF-5 and PGDF-5) could significantly enhance the osteogenic differentiation of MC3T3-E1 cells when cocultured with magnetic CaP microcarriers. Previous studies have shown that GDF-5 could promote osteogenic differentiation through the activation of ERK1/2 and p38 MAPK signaling pathways (Zhong et al., 2006). In this study, GDF-5 and PGDF-5 exhibited increased protein expressions of ALP, OCN and OPN, suggesting that bisphosphonate-treated GDF-5 had no negative effect on its bioactivity. Surprisingly, PGDF-5 demonstrated significantly enhanced osteogenic capability compared to GDF-5. This may be attributed to the osteogenic capability of bisphosphonates, which may enhance osteogenic differentiation through the activation of ERK and JNK signaling pathways (Fu et al., 2008, Safari et al., 2023). However, the underlying mechanism needs to be further investigated. Nevertheless, PGDF-5 modified magnetic CaP microcarriers could serve as an effective tool to enhance the osteogenic differentiation of cell aggregates.

### 3.5. The biological functions of endothelial cells cocultured with microcarrier extracts

Previous studies have shown that cell death tends to occur in the center of large-sized tissue constructs due to the hindrance caused by scaffold geometry, which limits the diffusion of nutrients (Xie et al., 2022, de Silva et al., 2023). Therefore, vascularization is considered a crucial factor that influences the formation of aggregates ranging from micrometers to millimeters or centimeters (de Silva et al., 2023). In this study, to evaluate the vascularization capability of the aggregates, HUVECs were introduced to coculture with microcarrier extracts. The immunofluorescent staining (Fig. 6A) showed that numerous cells cocultured with CaP/Fe$_3$O$_4$/GDF-5 and CaP/Fe$_3$O$_4$/PGDF-5 extracts expressed VEGF, whereas only a few cells cocultured with CaP and CaP/Fe$_3$O$_4$ expressed VEGF. Semi-quantitative analysis of VEGF fluorescence (Fig. 7D) showed a trend of CaP < CaP/Fe$_3$O$_4$ < CaP/Fe$_3$O$_4$/GDF-5 < CaP/Fe$_3$O$_4$/PGDF-5. All pairwise comparisons between the groups showed statistically significant differences (all p < 0.001). In addition, after coculture of 3 h, the number of meshes formed in the CaP/Fe$_3$O$_4$/PGDF-5 extract was significantly higher than that in the CaP and CaP/Fe$_3$O$_4$ groups (Fig. 7B and E). After coculture of 9 h, the number of meshes formed in the CaP/Fe$_3$O$_4$/PGDF-5 extract was significantly higher than that in the other three groups (Fig. 7B and E). Moreover, the scratch assay (Fig. 7C and F) showed that the extracts of CaP/Fe$_3$O$_4$/GDF-5 and CaP/Fe$_3$O$_4$/PGDF-5 had significantly positive effects on cell migration compared to the extracts of CaP and CaP/Fe$_3$O$_4$. Particularly, the cell migration rate was 43 % higher in the CaP/Fe$_3$O$_4$/PGDF-5 extract compared to the CaP/Fe$_3$O$_4$/GDF-5 extract, 157 % higher compared to CaP/Fe$_3$O$_4$ extract, and ~ 5.4 fold higher compared to CaP extract. These findings indicated that the addition of growth factors in
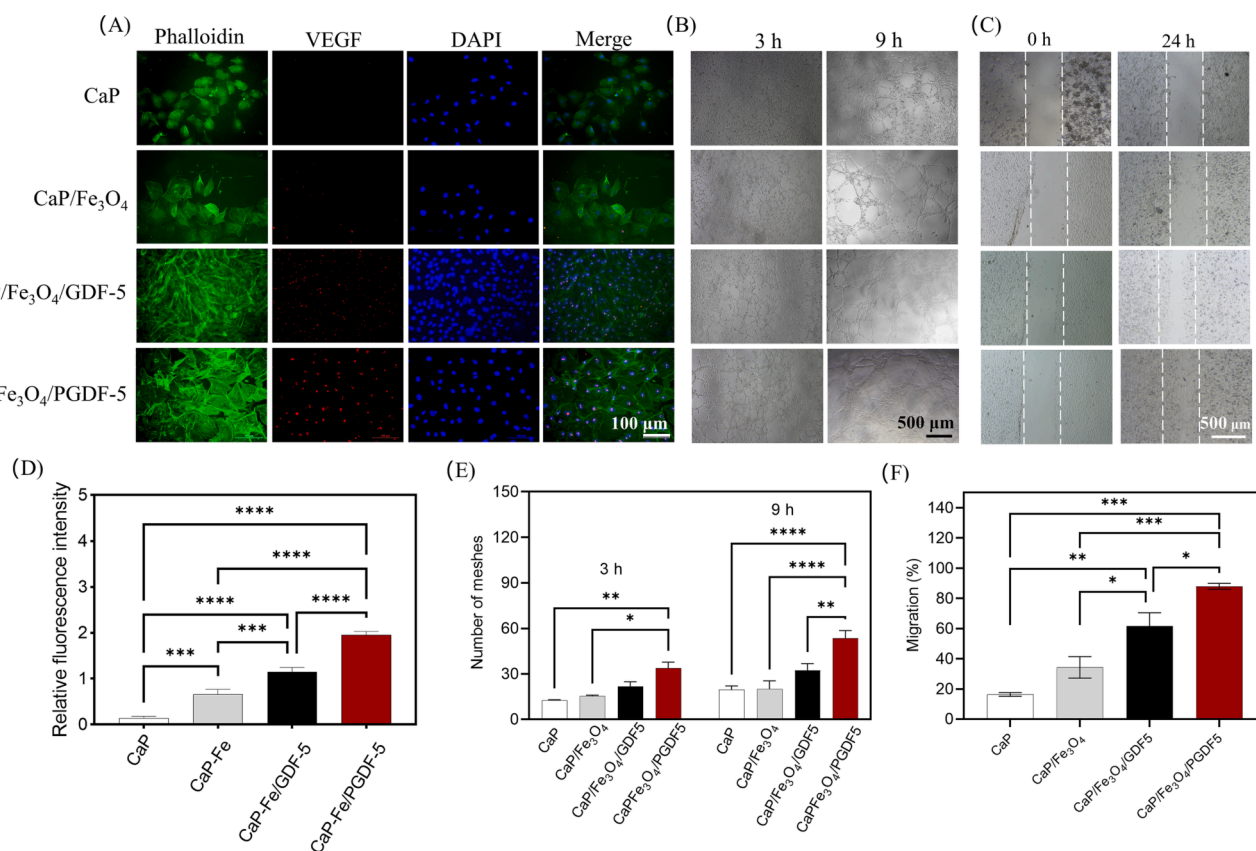
**Fig. 7.** Effects of different microcarrier extracts on biofunctionality of endothelial cells. (A) immunofluorescent staining of VEGF protein in HUVECs after co-culture with different microcarrier extracts for 4 d. F-actin was stained with iFluor488-labeled phalloidin (green), cell nuclei was stained using DAPI (blue) and VEGF was immunostained red, (B) tube-like network formation after coculture of HUVECs with different microcarrier extracts for 3 and 9 h, (C) cell migration evaluated by scratch assay, (D) semi-quantitative analysis of immunofluorescent staining of VEGF protein, (E) network formation quantified using number of meshes, (F) semi-quantitative analysis of the scratch assay. * represents $p < 0.05$, ** represents $p < 0.01$, *** represents $p < 0.001$,**** represents $p < 0.0001$.

the microcarriers could significantly enhance the migration and angiogenesis of endothelial cells, particularly in the case of CaP/Fe$_3$O$_4$/PGDF-5 microcarriers. Growth factor GDF-5 has been proved to induce angiogenesis *in vivo* (Yamashita et al., 1997) and enhance the angiogenic capability of BMSCs by increasing VEGF secretion *in vitro* (Kleinschmidt et al., 2013). In particular, the mutant GDF-5 protein BB-1, which incorporates BMP-2 residues into GDF-5, demonstrates both the osteogenic property of BMP-2 and the angiogenic property of GDF-5, thereby facilitating bone regeneration and spinal fusion (Kleinschmidt et al., 2013, Li et al., 2021). Similarly, PGDF-5 also exhibited positive effects on osteogenesis and angiogenesis, indicating its promising potential in bone regeneration.

Currently, microcarriers are always focused on the construction of microgels (e.g., gelatin, hyaluronic acid) that mimic the ECM microenvironment (Wu et al., 2015, Miszuk et al., 2021). However, hydrogel have limitations in terms of mechanical capacity and degradation rate, making them less suitable for repairing hard tissue (Leferink et al., 2014, Leferink et al., 2019, Luo et al., 2019). Moreover, the preparation of hydrogel-based microcarriers involves the use of potentially denaturizing or toxic crosslinking agents, which may create an unfavorable microenvironment for cell growth (e.g., UV irradiation and free radicals). Therefore, developing appropriate microcarriers for bone tissue repair need to be further studied. In this study, magnetic CaP-based microspheres were used as microcarriers, and a static culture system based on these microcarriers was found to be a promising tool for controlling the formation of cell spheroids. This approach exhibited how cells guided the assembly of microcarriers to form aggregates. In addition, to regulate the osteogenic and angiogenic capabilities of cells, we modified the surface chemistry of the microcarriers using growth

factors. Bisphosphonate-modified GDF-5 not only showed high affinity to CaP-base microcarriers, but also exhibited superior performance in promoting osteogenesis and angiogenesis.

However, controlling the assembly process for fabricating large-sized bone tissue constructions from the bottom up remains a challenge. In these days, magnetic particles have been widely used in biomedical fields due to their controllability and rapid response, which arise from the interactions between an external magnetic field and magnetic nanoparticles (Kianfar, 2021, Duong et al., 2022). In this study, we successfully assembled and fused isolated cell/microcarrier aggregates into larger structures from the bottom up with the assistance of an external magnetic field (Supplementary Fig. S9). However, without the aid of external magnetic field, this assembly process became significantly more difficult. The results demonstrate the potential benefits of using magnetic CaP-based microcarriers for the assembly of cell/microcarrier aggregates, which could be promising for constructing complex and large-sized bone tissue *in vitro*. In future studies, we will focus on coculturing various cells with the microcarriers and combining the cell/microcarrier assemblies with other instructive materials (such as hydrogel) as functional phases. This will allow us to further investigate their biofunctionality *in vivo* and explore their application and mechanism in bone regeneration.

## 4. Conclusions

In summary, this study reported a simple approach to prepare magnetic CaP-based microcarriers for bottom-up tissue engineering. These microcarriers could be assembled into large-sized tissue constructs with the guidance of cells. This approach not only imparts

magnetic properties to CaP microsphere, but also maintains the surface nanostructures. Additionally, the magnetic CaP microcarriers were further modified with bisphosphonate-modified GDF-5, which could enhance the affinity to CaP microcarriers and promote cell osteogenic and angiogenic properties. Overall, this study indicate that PGDF-5 modified magnetic CaP microspheres have the potential to be used as microcarriers in bottom-up bone tissue engineering, facilitating the construction of clinically relevant-sized tissue.

## Declaration of competing interest

The authors declare that they have no known competing financial interests or personal relationships that could have appeared to influence the work reported in this paper.

## Acknowledgements

## Appendix A. Supplementary material

Supplementary data to this article can be found online at https://doi.org/10.1016/j.arabjc.2024.105638.

## References

Achard, V., Martiel, J.L., Michelot, A., et al., 2010. A "primer"-based mechanism underlies branched actin filament network formation and motility. Curr. Biol. 20, 423–428.

Alipour, M., Aghazadeh, Z., Hassanpour, M., et al., 2022. MTA-enriched polymeric scaffolds enhanced the expression of angiogenic markers in human dental pulp stem cells. Stem Cells International 2022.

Bae, M.S., Ohe, J.Y., Lee, J.B., et al., 2014. Photo-cured hyaluronic acid-based hydrogels containing growth and differentiation factor 5 (GDF-5) for bone tissue regeneration. Bone 59, 189–198.

Costa, E.C., Gaspar, V.M., Coutinho, P., et al., 2014. Optimization of liquid overlay technique to formulate heterogenic 3D co-cultures models. Biotechnol. Bioeng. 111, 1672–1685.

De Silva, L., Bernal, P.N., Rosenberg, A., et al., 2023. Biofabricating the vascular tree in engineered bone tissue. Acta Biomater. 156, 250–268.

Dikina, A.D., Alt, D.S., Herberg, S., et al., 2018. Tissue engineering: a modular strategy to engineer complex tissues and organs. Adv. Mater. 5, 1870028.

Duong, H.T.K., Abdibastami, A., Gloag, L., et al., 2022. A guide to the design of magnetic particle imaging tracers for biomedical applications. Nanoscale 14, 13890–13914.

Feijao, T., Neves, M.I., Sousa, A., et al., 2021. Engineering injectable vascularized tissues from the bottom-up: Dynamics of in-gel extra-spheroid dermal tissue assembly. Biomaterials 279, 121222.

Froehlich, K., Haeger, J.D., Heger, J., et al., 2016. Generation of multicellular breast cancer tumor spheroids: comparison of different protocols. J. Mammary Gland Biol. Neoplasia 21, 89–98.

Fu, L., Tang, T., Miao, Y., et al., 2008. Stimulation of osteogenic differentiation and inhibition of adipogenic differentiation in bone marrow stromal cells by alendronate via ERK and JNK activation. Bone 43, 40–47.

Gibson, I.R., Bonfield, W., 2002. Novel synthesis and characterization of an AB-type carbonate-substituted hydroxyapatite. J Biomed Mater Res 59, 697–708.

Giles, G.I., Tasker, K.M., Jacob, C., 2001. Hypothesis: the role of reactive sulfur species in oxidative stress. Free Radic. Biol. Med. 31, 1279–1283.

Griffin, D.R., Weaver, W.M., Scumpia, P.O., et al., 2015. Accelerated wound healing by injectable microporous gel scaffolds assembled from annealed building blocks. Nat. Mater. 14, 737–744.

Gu, Y., Pinol, R., Moreno-Loshuertos, R., et al., 2023. Local temperature increments and induced cell death in intracellular magnetic hyperthermia. ACS Nano 17, 6822–6832.

Hori, M., Hagiwara, A., Goto, M., et al., 2021. Low-field magnetic resonance imaging: Its history and renaissance. Invest Radiol. 56, 669–679.

Hu, C., Gao, Z., Yang, X., 2006. Fabrication and magnetic properties of Fe3O4 octahedra. Chem. Phys. Lett. 429, 513–517.

Husain, S., Irfansyah, M., Haryanti, N., et al., 2019. Synthesis and characterization of Fe3O4 magnetic nanoparticles from iron ore. J. Phys.: Conf. Ser. IOP Publishing 1242, 012021.

James, A.W., LaChaud, G., Shen, J., et al., 2016. A review of the clinical side effects of bone morphogenetic protein-2. Tissue Eng Part B Rev. 22, 284–297.

Kianfar, E., 2021. Magnetic nanoparticles in targeted drug delivery: a review. J. Supercond. Nov. Magn. 34, 1709–1735.

Kleinschmidt, K., Ploeger, F., Nickel, J., et al., 2013. Enhanced reconstruction of long bone architecture by a growth factor mutant combining positive features of GDF-5 and BMP-2. Biomaterials 34, 5926–5936.

Koutsopoulos, S., 2002. Synthesis and characterization of hydroxyapatite crystals: a review study on the analytical methods. J. Biomed. Mater. Res.: Off. J. Soc. Biomater. Japanese Soc. Biomater. Australian Soc. Biomater. Korean Soc. Biomater. 62, 600–612.

Kumar, R., Sakthivel, R., Behura, R., et al., 2015. Synthesis of magnetite nanoparticles from mineral waste. J. Alloy. Compd. 645, 398–404.

Leferink, A., Schipper, D., Arts, E., et al., 2014. Engineered micro-objects as scaffolding elements in cellular building blocks for bottom-up tissue engineering approaches. Adv. Mater. 26, 2592–2599.

Leferink, A.M., Tibbe, M.P., Bossink, E., et al., 2019. Shape-defined solid micro-objects from poly(d, l-lactic acid) as cell-supportive counterparts in bottom-up tissue engineering. Mater. Today Bio. 4, 100025.

Leung, B.M., Sefton, M.V., 2010. A modular approach to cardiac tissue engineering. Tissue Eng. Part A 16, 3207–3218.

Li, L., Ling, Z., Vater, C., et al., 2021. GDF-5 variant loading on composite scaffolds promotes spinal fusion through coupling of osteogenesis and angiogenesis: A preclinical study in rhesus monkeys. Smart Mater. Med. 2, 322–333.

Luo, C., Fang, H., Zhou, M., et al., 2019. Biomimetic open porous structured core-shell microtissue with enhanced mechanical properties for bottom-up bone tissue engineering. Theranostics 9, 4663–4677.

Miszuk, J., Z, Liang., J Hu., et al., 2021. An Elastic Mineralized 3D Electrospun PCL Nanofibrous Scaffold for Drug Release and Bone Tissue Engineering. ACS Appl Bio Mater. 4, 3639-3648.

Mthembu, S.N., Sharma, A., Albericio, F., et al., 2020. Breaking a couple: disulfide reducing agents. Chembiochem 21, 1947–1954.

Oryan, A., Alidadi, S., Moshiri, A., et al., 2014. Bone morphogenetic proteins: A powerful osteoinductive compound with non-negligible side effects and limitations. Biofactors 40, 459–481.

Ouyang, L., Armstrong, J.P.K., Chen, Q., et al., 2020. Void-free 3D bioprinting for in-situ endothelialization and microfluidic perfusion. Adv. Funct. Mater. 30, 1909009.

Qi, M., Yao, S., Liu, X.C., et al., 2020. Nanosheet-assembled carbonated hydroxyapatite microspheres prepared by an EDTA-assisted hydrothermal homogeneous precipitation route. CrstEngComm 22, 2884–2888.

Raha, S., Ahmaruzzaman, M., 2021. Novel magnetically retrievable In2O3/MoS2/Fe3O4 nanocomposite materials for enhanced photocatalytic performance. Sci. Rep. 11, 6379.

Reddy, P.M., Chang, K.C., Liu, Z.J., et al., 2014. Functionalized magnetic iron oxide (Fe3O4) nanoparticles for capturing gram-positive and gram-negative bacteria. J. Biomed. Nanotechnol. 10, 1429–1439.

Safari, B., Aghazadeh, M., Aghanejad, A., 2023. Osteogenic differentiation of human adipose-derived mesenchymal stem cells in a bisphosphonate-functionalized polycaprolactone/gelatin scaffold. Int. J. Biol. Macromol. 241, 124573.

Safarpour, H., Banadkoki, S.B., Keshavarzi, Z., et al., 2017. Expression analysis and ATR-FTIR characterization of the secondary structure of recombinant human TNF-α from Escherichia coli SHuffle® T7 Express and BL21 (DE3) cells. Int. J. Biol. Macromol. 99, 173–178.

Safarzadeh, M., Ramesh, S., Tan, C.Y., et al., 2019. Effect of multi-ions doping on the properties of carbonated hydroxyapatite bioceramic. Ceram. Int. 45, 3473–3477.

Schmidt, T., Xiang, Y., Bao, X.J., et al., 2021. A paradigm shift in tissue engineering: From a top-down to a bottom-up strategy. Processes 9, 935.

Svitkina, T., 2018. The actin cytoskeleton and actin-based motility. Cold Spring Harb. Perspect. Biol. 10, a018267.

Tajima, S., Tabata, Y., 2018. Preparation of cell aggregates incorporating gelatin hydrogel microspheres containing bone morphogenic protein-2 with different degradabilities. J. Biomater. Sci. Polym. Ed. 29, 775–792.

Wang, Z., Wang, H., Xiong, J., et al., 2021. Fabrication and in vitro evaluation of PCL/gelatin hierarchical scaffolds based on melt electrospinning writing and solution electrospinning for bone regeneration. Mater. Sci. Eng. C Mater. Biol. Appl. 128, 112287.

Wright, J.E.I., Gittens, S.A., Bansal, G., et al., 2006. A comparison of mineral affinity of bisphosphonate–protein conjugates constructed with disulfide and thioether linkages. Biomaterials 27, 769–784.

Wu, A.T., Aoki, T., Sakoda, M., et al., 2015. Enhancing osteogenic differentiation of MC3T3-E1 cells by immobilizing inorganic polyphosphate onto hyaluronic acid hydrogel. Biomacromolecules 16, 166–173.

Xiao, D., Zhou, X., Li, H., et al., 2015. Fabrication of hollow hydroxyapatite particles assisted by small organic molecule and effect of microstructure on protein adsorption. J. Eur. Ceram. Soc. 35, 1971–1978.

Xiao, D., Guo, T., Yang, F., et al., 2017. In situ formation of nanostructured calcium phosphate coatings on porous hydroxyapatite scaffolds using a hydrothermal method and the effect on mesenchymal stem cell behavior. Ceram. Int. 43, 1588–1596.

Xiao, D., Zhang, J., Zhang, C., et al., 2020. The role of calcium phosphate surface structure in osteogenesis and the mechanisms involved. Acta Biomater. 106, 22–33.

Xie, C., Liang, R., Ye, J., et al., 2022. High-efficient engineering of osteo-callus organoids for rapid bone regeneration within one month. Biomaterials 288, 121741.

Yamashita, H., Shimizu, A., Kato, M., et al., 1997. Growth/differentiation factor-5 induces angiogenesisin vivo. Exp. Cell Res. 235, 218–226.

Yao, S., Qi, M., Qi, L., et al., 2021. Investigation of EDTA concentration on the size of carbonated flowerlike hydroxyapatite microspheres. R. Soc. Open Sci. 8, 202148.

Zarkesh, I., Ghanian, M.H., Azami, M., et al., 2017. Facile synthesis of biphasic calcium phosphate microspheres with engineered surface topography for controlled delivery of drugs and proteins. Colloids Surf. B Biointerfaces 157, 223–232.

Zhang, C., Yang, F., Xiao, D., et al., 2020. Repair of segmental rabbit radial defects with Cu/Zn co-doped calcium phosphate scaffolds incorporating GDF-5 carrier. RSC Adv. 10, 1901–1909.

Zhong, Z.M., Chen, J.T., Zhang, Y., et al., 2006. Growth/differentiation factor-5 induces osteogenic differentiation of human ligamentum flavum cells through activation of ERK1/2 and p38 MAPK. Cell. Physiol. Biochem. 26, 179–186.